

Stratified Sampling Based Compressed Sensing for Structured Signals

Theresa Loss , Matthew J. Colbrook , and Anders C. Hansen 

Abstract—Structured compressed sensing takes signal structure into account, thereby outperforming earlier compressed sensing methods. However, results are usually based on sampling in the Fourier domain, such as in Magnetic Resonance Imaging. In the time domain, the benefits of structured compressed sensing are still unknown. This paper introduces concepts that incorporate the signal structure into both the acquisition and reconstruction of compressed sensing in time and image domain applications. First, a stratified-random sampling pattern is proposed to improve the recovery of the dominant low-frequency range of natural signals. A heuristic *decay of primes* criterion is developed to evaluate the properties of the sensing matrix and is used to optimize the sampling pattern. Second, the sparsity of the Fourier transform as the representation domain is improved by estimating the signal structure in a preprocessing step, and then adapting the grid of the Fourier transform. In contrast to existing methods, *grid stretching* is integrated into the fast Fourier transform to reduce computational complexity. Both structured acquisition and reconstruction are evaluated using simulations, as well as two real-world applications: wireless sensor networks in structural health monitoring and electron microscopy. Results show that both reconstruction errors and robustness can significantly be improved by incorporating structure into the acquisition and reconstruction.

Index Terms—Electron microscopy, structured compressed sensing, stratified random sampling, structural health monitoring.

I. INTRODUCTION

TECHNOLOGICAL advances in physical and biological sensing applications frequently result from the need to overcome restrictions on the number of measurements taken by the system. Such restrictions may result from: a limited power supply, as present in wireless sensor networks [1]; limited measurement time, such as the duration of examination in Magnetic Resonance Imaging (MRI) [2]; as well as restrictions in energy doses in Electron Microscopy (EM) [3].

Manuscript received 8 March 2021; revised 16 February 2022 and 17 May 2022; accepted 1 June 2022. Date of current version 15 July 2022. The associate editor coordinating the review of this manuscript and approving it for publication was Dr. Marco Felipe Duarte. This work was supported in part by the Austrian Research Promotion Agency FFG, Research Partnerships under Grant 862437 and in part by company eologix sensor technology (T.L), a Research Fellowship at Trinity College, Cambridge (M.J.C.), a Leverhulme Prize and a Royal Society University Research Fellowship (A.C.H.). (*Corresponding author: Theresa Loss.*)

Theresa Loss is with the Institute of Electrical Measurement and Sensor Systems, Graz University of Technology, 8010 Graz, Austria (e-mail: loss.theresa@web.de).

Matthew J. Colbrook and Anders C. Hansen are with the Department of Applied Mathematics and Theoretical Physics, University of Cambridge, Cambridge CB2 1TN, U.K. (e-mail: m.colbrook@damtp.cam.ac.uk; ach70@cam.ac.uk).

Digital Object Identifier 10.1109/TSP.2022.3184162

Apart from tackling the problem from the hardware side, signal processing methods can be applied to reconstruct measurements from far fewer samples than the Nyquist criterion suggests. By exploiting sparseness of the original signal, compressed sensing (CS) has successfully been used in the last 15 years to solve the underdetermined inverse problem of reconstruction in many applications [4]–[7]. Recently, artificial intelligence has also been used in sampling problems, with neural networks (NNs) trained to optimally reconstruct original signals from a limited number of measurements [8], [9]. However, there remain several challenges with this approach:

1. The optimal trade-off between stability and accuracy of NNs is mostly unexplored [10], [11], and there is evidence that many current AI technologies may be unstable [10], [12]–[20] in a variety of scenarios. For example, it has been shown that tiny perturbations or structural changes in the image signal can lead to major changes in NN reconstruction [17].
2. The problem of false negatives is important in clinical practice. For example, Facebook and NYU’s 2019 FastMRI challenge reported that networks that performed well in terms of standard image quality metrics were prone to false negatives and failing to reconstruct small, but physically relevant image abnormalities [21]. The 2020 version of the challenge subsequently focused on pathologies, noting the problem of *AI-generated hallucinations* [22].
3. Reconstruction accuracy of a trained NN does not necessarily increase (and may in fact decrease) with an increased subsampling ratio. Typically, NNs need to be trained separately for varying subsampling ratios [17] (and on large training sets), which is computationally very expensive.

In this paper, we focus on so-called structured CS, which takes the signal’s sparse structure into account in both acquisition of measurements and reconstruction of the original signal. Despite the success of structured CS [23]–[34], including an abundance of elaborated theory, there is a lack (see §I-A) of structured CS-based strategies on how to incorporate structure into the acquisition of signals or images in time or image domains. This leads to the following crucial – and largely unexplored – question:

Question 1: *How to best incorporate structured sampling when sampling in the time or image domain?*

Mathematically, in the finite-dimensional case, this means that we have a reconstruction problem of the following form

$$\text{Given } y = P_{\Omega}x + e \in \mathbb{C}^m, \text{ recover } x \in \mathbb{C}^N, \quad (1)$$

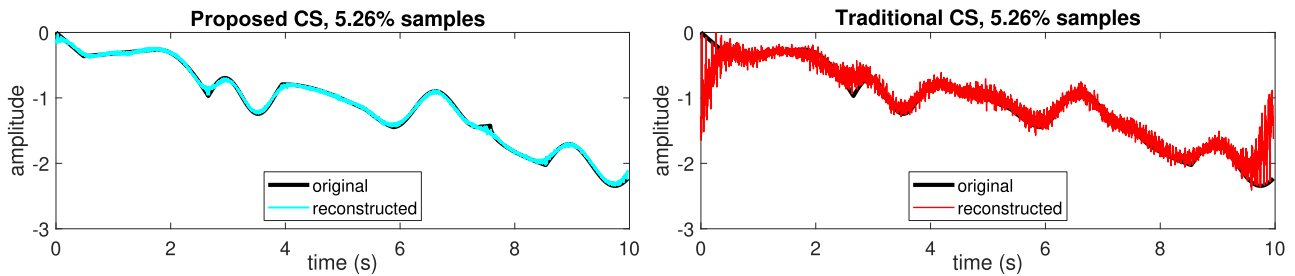


Fig. 1. Comparison of reconstruction results for the proposed method (“Proposed” CS, left) and current state-of-the-art CS (“Traditional” CS, right). Reconstruction from 5.26% of samples for a piecewise linear function with sampling for both methods in the time domain and reconstruction in the Fourier domain. Traditional CS uses uniform at random sampling in the time domain, whereas our proposed method uses structured sampling in the time domain and reconstruction via an adapted Fourier transform. Methods are presented in detail in the remainder of this paper (this example uses the model in §II-A with $N = 4000$).

where P_Ω is the operator choosing m components of x according to the index set $\Omega \subset \{1, \dots, N\}$ with $|\Omega| = m$ and $e \in \mathbb{C}^m$ is the noise vector. The big question is how to best choose Ω , and obviously that has to depend on the signal model. In this paper, we introduce *stratified subsampling*. On certain classes of structured signals, this strategy is much more effective than standard uniform sampling, as demonstrated in Fig. 1. Results are demonstrated by means of two applications, namely electron microscopy (EM) and the relatively new field of structural health monitoring (SHM). However, methods are not limited to those fields and we shall provide benefits for time- and image-domain-based sensing in many applications.

A. Related Work

Structured CS [23]–[34] has almost exclusively been developed for Fourier, Hadamard and Radon measurements in MRI, EM, CT etc. (for a comprehensive overview see [34] and the references therein), but not for sampling a signal or image directly in time or image (pixel) domain. Hence, there is very little literature to cite on this fundamental problem. One approach to be mentioned here is the so-called *spotscan* mode of acquisition as studied in [3], [35] to prevent damage by the electron beam. The classical setup for structured CS based on asymptotic incoherence and asymptotic sparsity is reviewed below. As we describe, the theory for this model is insufficient in our case, as there is no asymptotic incoherence nor any structured robust nullspace property in levels [26], [34] which are essential for this theory.

II. PROBLEM STATEMENT

A. Background – Standard Structured Sampling

Following, for example [23], [34], we consider briefly the following standard setup in structured sampling CS (see [34] for details). We are given the inverse problem

$$y = \Phi x, \quad x \in \mathbb{C}^N, \Phi \in \mathbb{C}^{N \times N},$$

where Φ typically has full rank. However, we cannot afford to sample all the components of y . If x is a natural image then Ψx is *asymptotically sparse* [34] when $\Psi \in \mathbb{C}^{N \times N}$ is a discrete wavelet transform (DWT). If, in addition, $\Phi \Psi^{-1}$ is *asymptotically incoherent* [34], one can sample a set $\Omega \subset \{1, \dots, N\}$ in

a random, yet structured, way with $|\Omega| = m \ll N$, based on the asymptotic incoherence and asymptotic sparsity and solve

$$\operatorname{argmin}_{\tilde{x} \in \mathbb{C}^n} \|\Psi \tilde{x}\|_1 \quad \text{s.t.} \quad \|P_\Omega y - P_\Omega \Phi \tilde{x}\|_2 \leq \epsilon, \quad (2)$$

with ϵ being a threshold, e.g. used to account for measurement noise (see [36] for computational issues regarding (2)). If Ω is chosen, for example, according to a multi-level sampling pattern as in Definition 1 (below) based on the asymptotic incoherence and asymptotic sparsity, one can substantially outperform uniform random sampling. Note that $\Phi \Psi^{-1}$ is always asymptotically incoherent when Φ is either the discrete Fourier transform (DFT) or the Hadamard transform (with certain specific orderings) and Ψ is a DWT [34, Ch. 11].

In our approach, we focus on the acquisition of measurements in the time or image domain and on sparse representation in the Fourier domain. Throughout, Ψ is taken to be the DFT so that

$$(\Psi x)[k] = X[k] = \sum_{n=0}^{N-1} x[n] e^{\frac{2\pi i n k}{N}}, \quad (3)$$

for $k = 1, \dots, N$ (see also §III-B for suitable adaptations).

B. Problem: Standard Theory and Methods Will Not Work

In our case we have

$$\Phi = I \Rightarrow I \Psi^{-1} \text{ is not asymptotically incoherent,}$$

and thus there is no known method for doing structured sampling. Our proposed method of stratified sampling is a proof-of-concept of this method and mathematical proofs of performance are not developed yet. However, we demonstrate substantial benefits over random sampling as illustrated in Fig. 1. Note that because of the lack of asymptotic incoherence, a standard multilevel sampling scheme used on the example in Fig. 1 (right) would give highly inaccurate results. In our proof-of-concept, we use a Monte Carlo simulation to create the sampling patterns and we leave mathematical theory to future developments.

C. Signal Model – Dominating Low Fourier Frequencies

In physical and biological sensing applications, many signals exhibit significant structure and are dominated by the low frequency range. Considering our two exemplary applications, we find that a sensor in an SHM application will typically

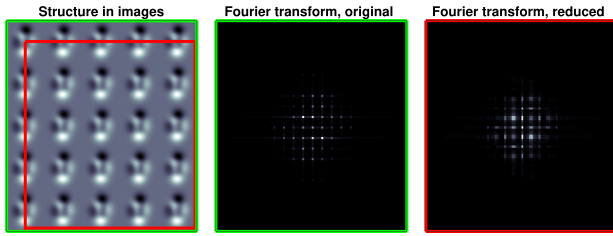


Fig. 2. Exemplary structure of an electron microscopy image (left). A magnified section of the Fourier coefficients is shown for the Fourier transform computed on (i) the original image (middle, green) and (ii) the section of the image (right, red).

measure the fundamental frequency of an oscillation and multiples thereof, complemented by the structure's eigenfrequencies. Also, EM images of materials and biological tissues exhibit significant regularities as modeled in Fig. 2, which shows reduced sparsity of Fourier coefficients if the underlying section of the image is misaligned with the signal structure.

We use \mathcal{S} to denote the indices corresponding to non-zero components of X . Our model assumption is that the signal X is sparse (or approximately sparse) for frequencies $k > K$ and some positive K (i.e., dominated by the low-frequency range). This leads to a refined version of Question 1 above:

Question 2: *How do we best incorporate structured sampling when sampling in time or image domain and the signal/image has dominating low frequencies – is uniform random sampling optimal?*

D. Structure in Acquisition

Unlike the case of sensing in the Fourier domain, mathematical principles on structured sampling in time- and image-domain-based sensing problems have, to our knowledge, not yet been developed. Since low frequencies dominate the signals in both applications, the following questions should be addressed when designing the sampling pattern:

- 1) How should we choose the sampling pattern Ω to capture a certain frequency?
- 2) How should we choose the sampling pattern Ω to ensure that the dominant lower frequencies in the signal are captured?
- 3) Repeat the above questions and ask additionally for robust (in terms of noise) reconstruction?

Our initial answers in §III-A to these questions are used to improve the design of the sensing matrix for a structured input signal.

E. Structure in Reconstruction

Additionally, the signal structure plays a major role when reconstructing signals from real-world discrete measurements. When using the DFT as the representation domain Ψ , the fast Fourier transform (FFT) is widely used to rapidly compute the Fourier transform of the discrete input signal. This leads to two major implications.

First, measurement devices are limited in terms of time and memory, and only capture a section of the original signal,

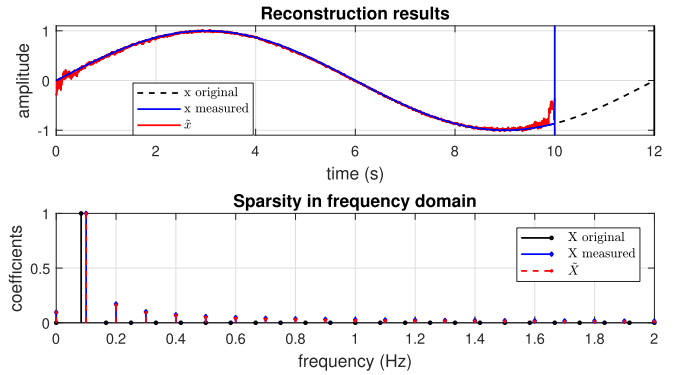


Fig. 3. Impact of window mismatch in the time domain (top) on the sparsity of Fourier coefficients (bottom). Reconstruction results are shown for a fundamental frequency of 0.083 Hz, sampled at 400 Hz, in the case of window mismatch for a measurement period of 10 s. \hat{x} denotes the solution of the optimization problem in (2) and \hat{X} denotes the frequencies $\Psi\hat{x}$.

which leads to discontinuities. Simultaneously, the FFT assumes periodic continuation of the input signal, which may lead to a mismatch between the measurement window and the signal structure. Fig. 3 shows the reconstruction results in case of window mismatch for a fundamental frequency of 0.083 Hz, and a measurement period of 10 s.

Second, *window mismatch* also implies *grid mismatch*. The resolution R of the signal is defined by the measurement window T with $R=1/T$, $T=t_N-t_1$ and t_n being the measurement time of samples $n \in \{1, \dots, N\}$. Hence, the alignment of the equally spaced frequency grid of the DFT to the signal structure depends on the measurement window as shown in Fig. 2 and Fig. 3 (bottom). A refinement of the discretization can help to align the signal structure to the grid. However, the resulting interpolation of the Fourier coefficients leads to decreased sparsity and should be avoided.

Therefore, we aim to incorporate the signal structure into reconstruction by answering the following questions:

- i) How can the structure of the signal be estimated from compressed measurements?
- ii) How can window and grid mismatch be addressed?
- iii) What adaptations can be made to the FFT to increase reconstruction accuracy while keeping computational costs low?

Our answers in §III-B to these questions are used to optimize the sparse representation Ψ and improve reconstruction.

III. MAIN RESULTS

This section contains the main results on incorporating the signal structure into the design of the sampling matrix during acquisition (§III-A) and into the sparsifying transform during the reconstruction of the signal (§III-B).

A. Sampling Algorithm

1) *Motivation:* The naive sampling approach would be to use uniform sampling with the sampling frequency f_s exceeding the highest dominant frequency $f_i=K$ in the spectrum by at least twice for exact recovery ($f_s \geq 2f_i$) [37]. Suppose that

$N/(2K) \in \mathbb{Z}$ and that we select every $N/(2K)$ th sample (so that $\Omega = \{lN/(2K) : l = 0, \dots, 2K - 1\}$). Consider two signals x_1 and x_2 such that the corresponding X_1 and X_2 differ only for indices $i_1 = r$ ($0 \leq r < K$) and $i_2 = 2K + r$, and such that $X_1[i_1] = X_2[i_2] \neq 0$ and $X_1[i_2] = X_2[i_1] = 0$. It follows that $y_1 = y_2$ and consequently reconstruction of compressed measurements fails.

To overcome this issue the first step is to make sure that $A = P_\Omega \Psi^* P_S$ is injective. From Theorem 1.1 in [7] we know that as long as $|\Omega| \geq 2|\mathcal{S}|$, this will be the case for any Ω and any \mathcal{S} when N is a prime. Such a luxury is rare in applications. However, there is a moral lesson from this result, as the phenomenon above would not happen for $\mathcal{S} = \{1, \dots, K\}$ when N is a prime as the sampling points will not form subgroups of $\mathbb{Z}/N\mathbb{Z}$, and avoiding such subgroups is thus a crucial motivation. This well-known problem is overcome to some degree by using uniform at random (UAR) sampling. However, if we have the extra structure where for example $\mathcal{S} = \{1, \dots, K\}$, we should be able to do better, which motivates our concept of stratified sampling.

2) *Stratified Sampling*: Since our signal model is dominated by the low-frequency range, we focus on the recovery of those frequencies. We propose a *stratified* sampling pattern, in which the maximum distance between adjacent samples is restricted. To introduce this, we first discuss multilevel sampling.

Definition 1 (Multilevel subsampling [23]): Let $\mathbf{N} = (N_1, \dots, N_l) \in \mathbb{Z}_{>0}^l$, where $0 \leq N_1 < \dots < N_l = N - 1$ and $\mathbf{m} = (m_1, \dots, m_l) \in \mathbb{N}^l$ with $m_k \leq N_k - N_{k-1}$ for $k = 1, \dots, l$, and $N_0 = 0$. For each $k = 1, \dots, l$, let $\mathcal{I}_k \subset \{N_{k-1} + 1, \dots, N_k\}$ with $|\mathcal{I}_k| = m_k$. We refer to $\mathcal{I}_1 \cup \dots \cup \mathcal{I}_l$ as an (\mathbf{N}, \mathbf{m}) -multilevel subsampling scheme.

In Definition 1, the vector \mathbf{N} describes the levels and \mathbf{m} describes the sparsities in each level. The \mathcal{I}_k denote possible index sets that satisfy the corresponding subsampling scheme. For equidistant batch length L and a fixed number of samples m per batch, we introduce stratified subsampling, which becomes a particular type of multilevel sampling.

Definition 2 (Stratified subsampling): Let $\lambda > 0$, $L(K, \lambda) = \lceil N/(2K\lambda) \rceil$ (batch length) and $l = \lceil N/L(K, \lambda) \rceil$ (number of batches). For $k = 1, \dots, l - 1$, set $N_k = k \cdot L(K, \lambda) - 1$ and set $N_l = N - 1$. If $m_1 = m_2 = \dots = m_l = m > 0$, we refer to an (\mathbf{N}, \mathbf{m}) -multilevel subsampling scheme as a stratified subsampling scheme. We set $M = m_1 + \dots + m_l$ and denote the set of such stratified subsampling schemes by $\Lambda(K, \lambda, m)$.

The constant λ is a multiplier which shrinks the batch length according to the number of samples in $\Omega \in \Lambda(K, \lambda, m)$. It has been selected empirically in the following experiments with a lower limit of $\lambda = 1$. We have also selected $m = 2$. In the following, we seek a deterministic sampling pattern that optimizes the positions of the samples within batches.

3) *Optimization of the Sampling Pattern*: Let $\Omega = \{s_1, s_2, \dots, s_M\} \in \Lambda(K, \lambda, m)$ be a stratified sampling pattern. The pairwise distances between elements in Ω can be calculated as $D_{K,m} = \{d_{i,j}\}$, with $d_{i,j} = s_j - s_i$ for $j > i$. We denote this list (which includes possible repeats) as $D_{K,m} = \{d_1, \dots, d_{L_D}\}$, where $L_D = m(m - 1)/2$.

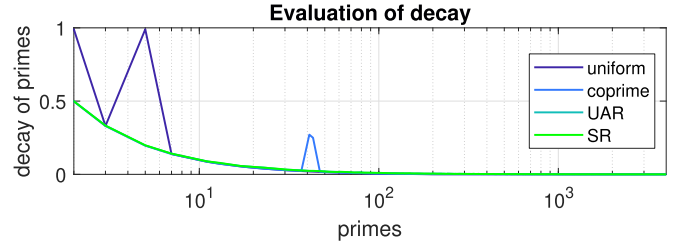


Fig. 4. Decay of multiples of primes $U_{K,m}(p)$ for pairwise distances $D_{K,m}$ for uniform sampling (*uniform*), coprime sampling (*coprime*), uniform at random sampling (*UAR*), and stratified sampling (*SR*). 5% sampling is used for $N = 4000$.

Let $\mathcal{P}_N = \{p_1, p_2, \dots, p_{L_P}\}$ be the collection of primes smaller than N and define, for each prime $p \in \mathcal{P}_N$,

$$U_{K,m}(p) := \frac{1}{L_D} \sum_{j=1}^{L_D} \nu_j, \quad \nu_j = \begin{cases} 1 & \text{if } d_j \bmod p = 0 \\ 0 & \text{else.} \end{cases} \quad (4)$$

In other words, the decay of primes $U_{K,m}(p)$ tells the proportion of elements of $D_{K,m}$ that are divisible by the prime p .

To avoid subgroups of $\mathbb{Z}/N\mathbb{Z}$ appearing in the set of distances, we desire that $U_{K,m}(p)$ is small. Smaller primes p will, as a rule of thumb, have larger $U_{K,m}(p)$ and have a greater chance of contributing to subgroups. We therefore desire that $U_{K,m}(p_{j+1}) - U_{K,m}(p_j)$ is small. Therefore, we introduce the following quantity:

$$Dc(\Omega) := \frac{1}{L_P} \sum_{j=1}^{L_P-1} \max \left\{ 0, \frac{U_{K,m}(p_{j+1}) - U_{K,m}(p_j)}{U_{K,m}(p_j)} \right\}. \quad (5)$$

The corresponding algorithm is shown in Algorithm 1. We then seek to solve the following optimization problem:

$$\min_{\Omega \in \Lambda(K, \lambda, m)} Dc(\Omega). \quad (6)$$

Constructing a deterministic stratified pattern Ω with minimum overall decay $Dc(\Omega)$, is a highly non-trivial task. Therefore, we use a Monte Carlo simulation to create a large number of stratified sampling patterns and select the pattern with minimum overall decay Dc (see Algorithm 2). In the simulation, stratified patterns are created by distributing samples uniformly at random per batch. This is referred to as *stratified-random* (SR) sampling in the following. Accordingly, the optimized pattern is denoted as *stratified-random-minimized* (SRM) pattern and described as $\Omega(K, N, q)$ for a signal length N and sampling quota $q = M/N$.

As an example, the decay $Dc(\Omega)$ is analyzed for four different sampling patterns with signal length $N = 4000$ and 5% of samples in Fig. 4. In the case of UAR and SR sampling, one can note a smooth decay with $U_{K,m}(p_i) > U_{K,m}(p_{i+1})$. On the other hand, uniform sampling results in two distinct peaks at $p=2$ and $p=5$. Additionally, *coprime* sampling has been analyzed, which uses two coprime integers p_1 and p_2 to determine the sampling pattern $\Omega = \Omega_1 \cap \Omega_2$, with $\Omega_i = np_i$ for $n = 1, \dots, N/p_i$ and $i = 1, 2$ [38]. Coprime sampling has successfully been used in the field of array sensing to find the optimal placement of single

Algorithm 1: Find the overall decay $Dc(\Omega)$.

```

function FINDDECAY(pattern)
  def D,U ▷ empty arrays
  for i = 1 to length pattern
    for j = i to length pattern
      if pattern[i] = 1 AND pattern[j] = 1 ▷ distance
        D.append(j-i) ▷ append list of distances
      end if
    end for
  end for
  def P = {1,2,3,5,7,...M} ▷  $M \leq N$ , all primes
  for i = 1 to length P
    for j = 1 to length D
      if D[j] mod P[i] = 0 ▷ find multiples
        U[i] = U[i]+1 ▷ create decay of primes
      end if
    end for
  end for
  def Dc = 0 ▷ initialize
  for i = 2 to length U
    if U[i]-U[i-1]>0 ▷ only use positive differences
      Dc = Dc+(U[i]-U[i-1])/U[i] ▷ sum decay
    end if
  end for
return Dc

```

Algorithm 2: Pattern creation by using Monte Carlo simulation.

```

function MINIMIZEMULTIPLESRPATTERN(K,M)
  def decayMIN = 100 ▷ initialize with large number
  for i = 1 to 1000 ▷ test 1000 patterns
    pattern = getPattern(K,M) ▷ SR pattern, §III-A2
    Dc = findDecay(pattern)
    if Dc ≤ decayMIN
      def patternOPT = pattern
      decayMIN = Dc
    end if
  end for
return patternOPT

```

measurements [38]–[40], but it results in an increase in multiples for the two primes as simulated here for $p_1 = 41$ and $p_2 = 43$.

4) *Numerical Evaluation:* In order to recover x from y , the matrix $A = P_\Omega \Psi^* P_S$ must be injective [34]. A useful quantity in this regard is the condition number $\kappa(C)$ with $C = A^*A$.

We simulate three different signal models with (i) exactly one non-zero frequency with $\mathcal{S} = \{K\}$, (ii) non-zero frequencies $k \leq K$ with $\mathcal{S} = \{1, \dots, K\}$ and (iii) low frequencies with two additional frequencies $\mathcal{S} = \{1, \dots, K, \frac{N}{4}, \frac{N}{2}\}$. The sensing matrix P_Ω is generated for UAR, SR and SRM sampling, and 1000 realizations each for different percentages q and $K = 8$ are tested. Results show that condition numbers are significantly smaller for SRM sampling than for UAR sampling (see Fig. 5).

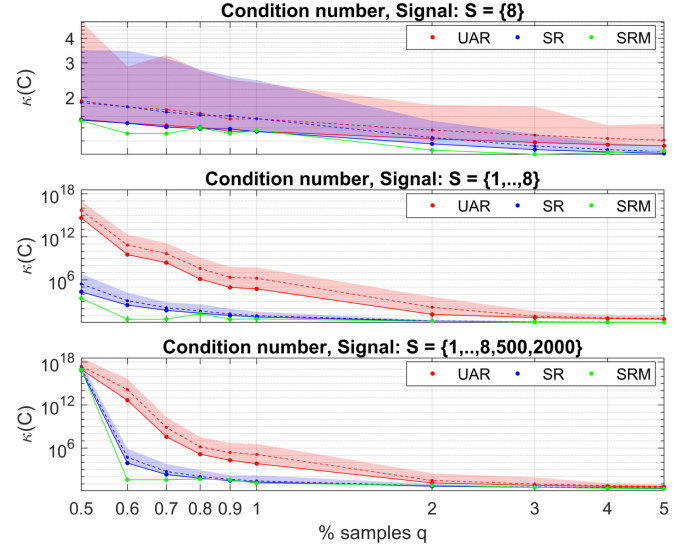


Fig. 5. Condition number $\kappa(C)$ visualized. Shaded areas, solid and dashed lines represent maximum, mean and mean with additional standard deviation of respective $\kappa(C)$ for 1000 realizations each. Results are shown for UAR, SR and SRM sampling with different percentages of samples q and signal length $N = 1000$. The low frequency range is set to $K = 8$. Three different signal models are simulated, Top: $\mathcal{S} = \{8\}$, Middle: $\mathcal{S} = \{1, \dots, 8\}$, Bottom: $\mathcal{S} = \{1, \dots, 8, 500, 2000\}$.

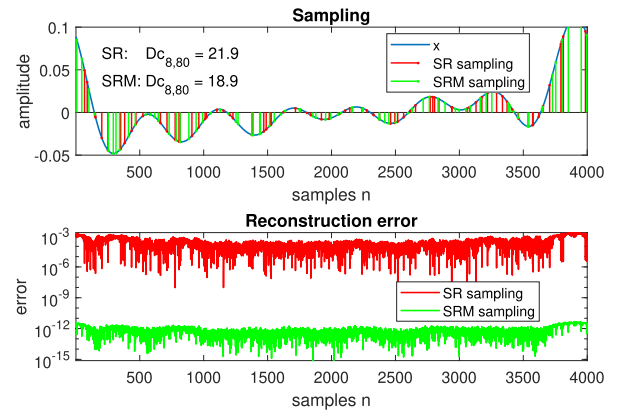


Fig. 6. Exemplary worst case scenario for SR sampling in comparison to SRM sampling. Top: Original signal with $\mathcal{S} = \{1, \dots, 8\}$, $N = 4000$, 2% of samples used, i.e. $M = 80$. The decay Dc is also shown. Bottom: Reconstruction error $\|x - \hat{x}\|$ on a logarithmic scale, where \hat{x} is reconstructed by using (i) SR sampling and (ii) SRM sampling.

Applying ℓ_1 -reconstruction as in (2) for all sampling patterns supports those findings. Fig. 6 displays a worst-case scenario for a signal model $\mathcal{S} = \{1, \dots, 8\}$, $N = 4000$ and 2% of samples being used. A comparison of SR and SRM sampling shows that reconstruction is significantly improved by using SRM sampling. In addition, reconstruction errors are evaluated for the three signal models, for which condition numbers have been compared, and UAR, SR and SRM sampling. Reconstruction results for different sampling percentages q and 1000 realizations each are displayed in Fig. 7 and demonstrate a reduction of reconstruction errors for SRM sampling in comparison to UAR sampling. Consequently, our proposed SRM sampling method can be used to improve the reconstruction results of structured signals at low sampling rates.

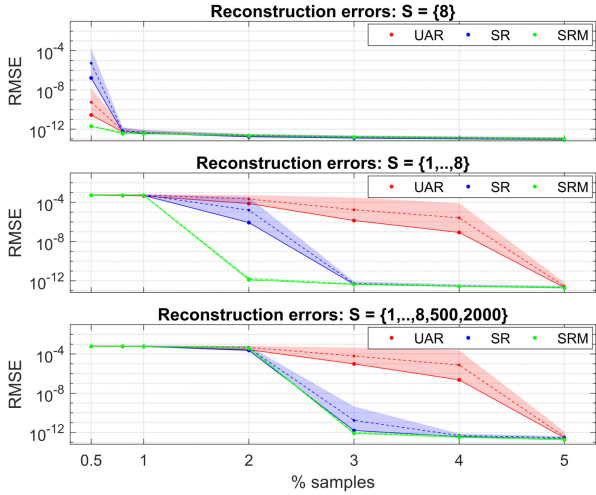


Fig. 7. Comparison of reconstruction results for UAR, SR and SRM sampling and different percentages of samples $q = \frac{M}{N}$, $N = 4000$. Solid lines, dashed lines and shaded areas represent the mean, the mean plus standard deviation and the maximum of root-mean-square errors (RMSE) in the time domain for 1000 realizations each. The three signal models are the same as described in Fig. 5.

5) *Main Findings*: Our findings on the design of a structured sampling pattern for adapting signal acquisition to the structure of the input signal can be summarized as follows:

- i) The direct transfer of structured sampling approaches in Fourier sensing to sensing in time or image domain is impossible.
- ii) The low frequency range can be considered by using stratified sampling, which restricts distances between adjacent samples.
- iii) By selecting a sampling pattern with minimum overall decay $D_c(\Omega)$, reconstruction accuracy can significantly be increased.

B. Structured Reconstruction

1) *Estimation of Signal Structure*: While a general knowledge of the signal structure is sufficient to design a suitable sampling pattern, e.g. focusing on the recovery of low frequencies, knowledge of the location of those frequencies improves reconstruction. Several approaches have been proposed for iteratively adapting the DFT via dictionary learning [41], [42]. However, this leads to a non-uniform grid, for which a fast implementation via the FFT is impractical. Our approach focuses on a feasible implementation for real-world applications based on the FFT as an implementation of the DFT, thereby reducing computational effort and memory consumption.

The signal structure can be estimated from under-sampled measurements $y = P_\Omega x$ by optimizing the representation Y resulting from $Y = \Psi_{\hat{N}} y$, where

$$(\Psi_{\hat{N}} y)[k] = Y[k] = \sum_{n=0}^{N-1} (P_\Omega x)[n] e^{\frac{2\pi i n k}{\hat{N}}} = \sum_{n \in \Omega} y[n] e^{\frac{2\pi i n k}{\hat{N}}}, \quad (7)$$

with $\hat{N} \geq N$ the size of the used DFT. Let $\epsilon > 0$ be a thresholding parameter and let I_1 denote the indices corresponding to coefficients of Y greater in magnitude than ϵ and I_0 be the

complementary indices. For an ideal sparse representation, we expect the following sparsity measure χ to be large,

$$\chi(\hat{N}) := \frac{|I_0|}{|I_1|} \sum_{j \in I_1} |Y_j| / \left(\sum_{j \in I_0} |Y_j| \right). \quad (8)$$

We can therefore select a DFT size which seeks to maximize χ over a suitable range of sizes

$$\max \chi(\hat{N}). \quad (9)$$

In many applications, prior knowledge on the signal structure is available based on simulations, construction plans, experiments, physical, chemical or biological properties etc. and can replace or support structure estimation in (9).

2) *Implementation*: We now discuss how to implement the optimization problem with regard to the DFT size \hat{N} . The optimization problem can be interpreted in two different ways:

- i) If $\hat{N} = cN$ with $c \in \mathbb{N}$, the optimization problem corresponds to c -fold subsampling. Subsampling can be used to adapt the DFT to the signal structure but is only successful if a large c is chosen. However, this comes along with increased computational effort and storage consumption while decreasing sparsity. Therefore, subsampling should not be used as a method on its own but can be used to complement structure estimation.
- ii) If $\hat{N} = \theta^{-1}N$ with $\theta^{-1} \in (1, 2)$, the optimization problem corresponds to stretching of the fixed grid of the DFT by a factor θ :

$$\sum_{n \in \Omega} x[n] e^{\frac{2\pi i n k}{\hat{N}}} = \sum_{n \in \Omega} x[n] e^{2\pi i \theta \frac{k}{N} n}. \quad (10)$$

For a harmonic signal model, i.e., $\mathcal{S} = \{f_0, 2f_0, 3f_0, \dots\}$, the size of the DFT can be estimated as

$$\hat{N} = \left\lceil \frac{f_s}{\hat{f}_0} \left\lceil N c \frac{\hat{f}_0}{f_s} \right\rceil \right\rceil \quad (11)$$

with f_s, \hat{f}_0 being the sampling frequency and the estimated fundamental frequency, respectively.

- iii) A combination of stretching and subsampling can be implemented by selecting $cN < \hat{N} < (c+1)N$ for $c \in \mathbb{N}$, e.g., to account for a harmonic signal model with a small number of higher non-harmonics, such as $\mathcal{S} = \{f_0, 2f_0, 3f_0, f_{i1}, f_{i2}\}$.

Fig. 8 shows the results for a comparison of those different implementation options by using an $\Omega(10, 4000, 10)$ SRM sampling pattern. In detail, *original* reconstruction with $c=1$, *stretching* with $1 \leq c < 2$, *subsampling* with $(c=3)$ and the combination of *stretch.+subsampl.* ($3 \leq c < 4$) are compared. If c comprises a range, the \hat{N} maximizing χ is picked. The input signal consists of multiples of a fundamental frequency f_0 and two additional frequencies $10 \leq f_i, f_j \leq 20$ Hz. Lowest reconstruction errors are achieved by combining the two methods of bin stretching and subsampling. In doing so, grid mismatch is reduced for harmonics by grid stretching and for non-harmonics

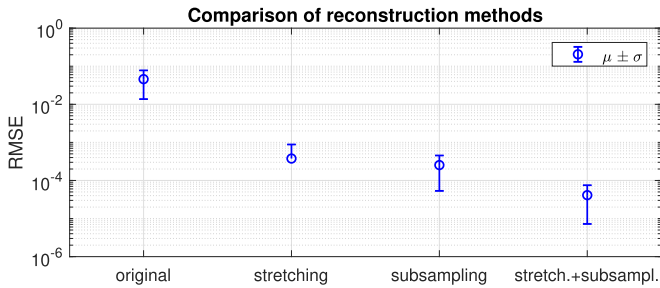


Fig. 8. Reconstruction results for *original*, *stretching*, *subsampling*, *stretch.+subsampl.* reconstruction and an $\Omega(10, 4000, 10)$ SRM pattern. The input signal consists of $\{f_0, 2f_0, 3f_0, f_i, f_j\}$ with randomly selected $0.1 \leq f_0 \leq 0.2$ Hz and $10 \leq f_i, f_j \leq 20$ Hz. Mean μ and standard deviation σ of root-mean-square errors (RMSE) displayed.

by subsampling. The computational effort remains small due to using the FFT.

3) Main Findings:

- i) The signal structure can be estimated by maximizing a sparsity measure. Estimation can be complemented by prior knowledge in many applications.
- ii) Window and grid mismatch can be addressed by adapting the representation matrix Ψ to the model of the signal by using a combination of stretching and subsampling.
- iii) To keep computational effort at bay, the FFT is used to compute Ψ . The number of frequency points is moderately increased up to the best match of estimated signal model and frequency grid.

IV. APPLICATIONS

In the following, our findings are demonstrated by means of two applications. First, structured CS is applied to the emerging field of SHM, in which measurements are conducted in the time domain (§IV-A). Second, structure is incorporated into CS of EM images which are acquired using time- and image-domain-based sensing (§IV-B).

A. Structural Health Monitoring

In the field of SHM, sensor networks are widely used to continuously monitor the condition of civil structures. Since sensors often operate wirelessly and depend on energy harvesting methods, CS is promising to reduce the energy needed for measurements as well as for wireless data transmission [43]–[45]. Even though vibration measurements in SHM applications are highly structured, signal structure is still being neglected in the vast majority of CS approaches.

In our example, we focus on CS in the field of wind turbines, in which continuous monitoring is essential to increase the safety and competitiveness of wind energy. By measuring vibrations of the turbine blades, blade damage can be detected and turbine settings can be optimized to reduce load and forces acting on the blades [46], [47].

The vibrational response of a turbine blade was measured in operation of the turbine by mounting triaxial accelerometers on the blade tip as described in [48]. To reduce the impact of noise at high rotation frequencies, only measurements at low rotation

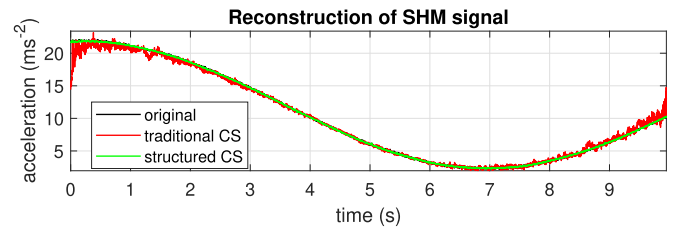


Fig. 9. Original and reconstructed acceleration, 10% of samples used. Comparison of (i) traditional CS (UAR sampling and reconstruction with original resolution, $\hat{N} = N$) and (ii) structured CS ($\Omega(10, 4000, q)$ SRM sampling, reconstruction with stretching and threefold subsampling, $3N \leq \hat{N} \leq 4N$).

frequencies ($f_0 \leq 0.15$ Hz) were evaluated. Also, the following analysis is based on measurements in x -direction of the sensor, which experienced the lowest noise levels. Acceleration was measured at 400 Hz for a duration of 10 s. The sampling matrix has not been integrated into the prototype sensor yet; therefore, compressed measurements are simulated and are selected from the set of measurements according to the sampling matrix.

Fig. 9 shows original and reconstructed acceleration for traditional CS with 10% of samples and *original* reconstruction, and structured CS with an $\Omega\{10, 4000, 10\}$ SRM pattern and *stretch.+subsampl.* reconstruction with $c = 3$. One can clearly note that the measured signal is dominated by the fundamental rotation frequency, which does not coincide with the measurement window. Consequently, *window mismatch* and resulting *grid mismatch* lead to poor reconstruction results for traditional CS. When using structured CS instead, the fundamental frequency is incorporated into reconstruction and, thereby, reconstruction accuracy at the boundaries of the measurement interval is improved significantly.

Next, the overall reconstruction accuracy is evaluated by calculating the following errors in the frequency domain:

- E1: Low-frequency error for $k \leq 10$ in the frequency domain.
- E2: Overall error across all frequencies.
- E3: Noise error: Distinct peaks in the original spectrum are identified. The error is then computed for all remaining frequencies to assess the number of falsely created peaks.
- E4: Peak error for the 10 peaks with largest amplitude.

Results for 100 measurement campaigns and the same parameter settings used in the single example in Fig. 9 are depicted in Fig. 10. Reconstruction errors for all error measures are reduced by using structured CS. To summarize, incorporating the signal structure into CS algorithms is beneficial in SHM applications such as monitoring of wind turbine blades.

B. 1D and 2D Imaging

CS is promising in imaging methods such as electron microscopy (EM), in which samples are acquired according to fixed positions in the image domain. By reducing the number of measurements, the risk of damaging sensitive structures can be reduced. Different variants of EM have incorporated CS methods, such as random-beam scanning transmission EM [49] and scanning line probe imaging [50]. In addition, CS has been used for further scanning microscopy methods such as fluorescence

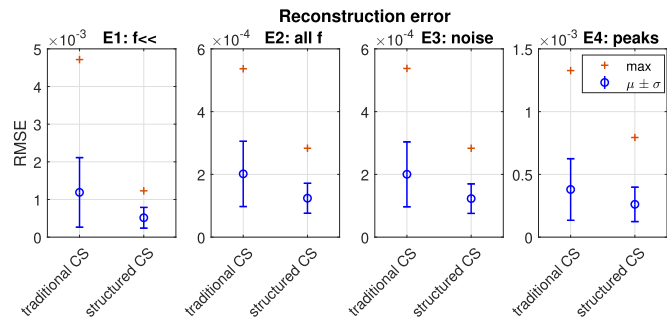


Fig. 10. Reconstruction errors for 100 acceleration measurement campaigns on the turbine for 10 s each. Comparison of (i) traditional CS (10 % UAR sampling, reconstruction with original resolution, $\hat{N} = N$) and (ii) structured CS ($\Omega(10, 4000, q)$ SRM sampling, reconstruction with stretching and threefold subsampling, $3N \leq \hat{N} \leq 4N$). Mean μ , standard deviation σ and maximum of root-mean-square errors (RMSE) are displayed.

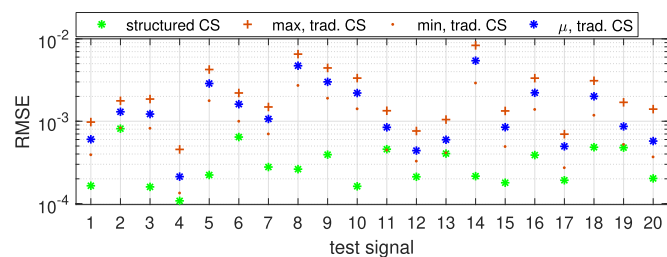


Fig. 11. Variability of reconstruction errors for traditional CS (5% UAR sampling, reconstruction with $\hat{N} = N$) in comparison to structured CS ($\Omega(10, 4000, 5)$ SRM sampling, structured reconstruction with $N \leq \hat{N} \leq 3N$). 20 one-dimensional images simulated (piecewise linear functions, signal length $N = 4000$) with 100 UAR patterns tested per image. Root-mean-square errors (RMSE) displayed.

microscopy [51] and atomic force microscopy [52]. Even though the implementation of the sensing matrix was optimized and adapted in a few approaches [52], [53], no specific attention has been paid to the design of the sensing matrix itself.

In the following, two experiments are performed for evaluating the benefit of structured CS for EM.

1) *Experiment 1 - 1D Evaluation of Structured CS:* First, the variability of UAR sampling in traditional CS is evaluated against fixed SRM sampling in structured CS. To reduce computational complexity, one-dimensional (1D) test signals are created by using piecewise linear functions. For this, the signal length $N = 4000$ is divided into 10 pieces with corresponding functions randomly selected from the set $F(x) = \{b \sin(2\pi ax), ax, a\sqrt{x} + b, b \cos(2\pi ax)\}$ and randomly selected parameters a and b from a Gaussian distribution. An additional offset is introduced to align the last value of each piece to the first value of the next one. In total, 20 one-dimensional images are simulated and 100 UAR patterns with 5% of samples are tested per signal. For structured CS, SRM sampling was selected with $\Omega(10, 4000, 5)$ and reconstruction with $N \leq \hat{N} \leq 3N$.

Results show that reconstruction errors for structured CS are smaller than for traditional CS for all test signals (see Fig. 11). Additionally, errors for traditional CS are highly variable both within and between test signals, with the maximum error of

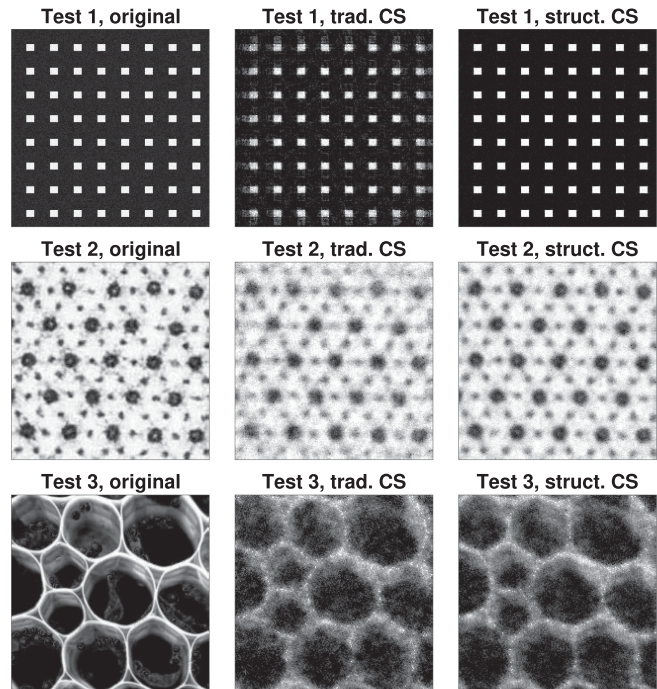


Fig. 12. Image reconstruction by using traditional CS, i.e. 10% UAR sampling with $\hat{N} = N$, and structured CS ($\Omega(10, 200, 10)$ SRM sampling, structured reconstruction with $3N \leq \hat{N} \leq 4N$). From left to right: (i) original images of size 200×200 , (ii) traditional CS and (iii) structured CS reconstruction. Top row: test image with 2% noise, relative L2 error 0.36 / 0.10 and PSNR 19.2 dB / 30.2 dB for traditional and structured CS, respectively. Middle row: EM image of animal cells, snippet from [54], rel. L2 error 0.16 / 0.13 and PSNR 17.5 dB / 19.3 dB. Bottom row: EM image of animal cells, snippet from [55], rel. L2 error 0.47 / 0.42 and PSNR 15.1 dB / 16.1 dB.

structured CS being 10 times smaller than the maximum error of traditional CS.

2) *Experiment 2 - 2D Test Images:* Next, the benefit of structured CS in EM is evaluated. When moving from 1D to 2D test signals, the design of the sampling matrix needs to be extended to two dimensions. For this, the concept of 1D batches in stratified subsampling is extended to 2D batches and the pairwise distance between elements in Ω are calculated as Euclidean distances $d_{i,j} = (d_i^2 + d_j^2)^{\frac{1}{2}}$. In addition, the signal structure is estimated by adapting the size $[\hat{N}_1, \hat{N}_2]$ of the two-dimensional DFT.

In order to demonstrate our method, one highly structured test image and two EM images of animal cells are tested (see Fig. 12). UAR sampling with 10% samples is compared with $\Omega(10, 200, 10)$ SRM sampling for the 200×200 images. Structured reconstruction with $3N \leq \hat{N} \leq 4N$ is used and the structure of the two-dimensional DFT is estimated as [695,623] (Image 1), [686,624] (Image 2) and [684,618] (Image 3) by using the 2D extension of equations 8 and 9.

For the test image (Image 1), reconstruction errors can be decreased significantly by 72% from 0.36 to 0.10. In addition, the peak signal-to-noise ratio (PSNR) was used to evaluate reconstruction results by relating the peak amplitude \hat{a} of the original image to the reconstruction error $e = \sqrt{(I_{orig} - I_{rec})^2}$ between original and reconstructed image I with $psnr = 20 \log(\frac{\hat{a}}{e})$. For

the test image, the PSNR could be increased significantly by 11.0 dB from 19.2 dB to 30.2 dB.

For the real-world EM images, structure is not as prominent as for the 1D SHM application. Consequently, reconstruction accuracy is increased by 18.5% (from 0.16 to 0.13) and 10.6% (from 0.47 to 0.42), and PSNRs are increased by 1.8 dB (from 17.5 dB to 19.3 dB) and 1.0 dB (from 15.1 dB to 16.1 dB) for Image 2 and Image 3, respectively, by using structured CS.

As for the 1D case, structured CS is expected to increase robustness but either needs computationally costly Monte Carlo simulations or profound mathematical elaboration to be verified. This exceeds the scope of this paper and will be covered in future work. One needs to note that in our applications images are sampled by picking single locations as needed in EM. This is a different task than in many image reconstruction problems, in which Fourier sensing is paired with reconstruction by using wavelets. Therefore, results cannot be compared to those reconstruction problems one-by-one.

V. CONCLUSION

Even though structured CS is state-of-the-art in Fourier sensing applications, structure is still neglected in most time- and image-domain-based sensing applications. In this paper, we developed a method to incorporate structure into both the acquisition of samples and the reconstruction of signals, thereby significantly reducing reconstruction errors in such applications. The sensing matrix was designed via stratified random sampling with the sample intervals being related to the largest frequency being captured. Also, a measure for optimizing the sampling pattern was proposed to increase the robustness of reconstruction. Additionally, we propose structured reconstruction for reducing grid mismatch of the Fourier transform while keeping computational costs low.

Simulation results show that structured CS significantly reduces reconstruction errors and increases robustness. Structured CS also successfully reduces reconstruction errors in an SHM application. Error reduction was smaller in 2D EM and we propose further research on the estimation of signal structure in 2D images in the future. Our approach represents first steps from structured Fourier sensing to time- and image-domain-based sensing, and we hope that it will initiate further work on structured sampling and how it can be generalized.

ACKNOWLEDGMENT

T.L. wishes to thank the Department of Applied Mathematics and Theoretical Physics, University of Cambridge, for hosting a research stay during which work for this paper took place.

REFERENCES

- [1] G. Anastasi, M. Conti, M. Di Francesco, and A. Passarella, "Energy conservation in wireless sensor networks: A survey," *Ad Hoc Netw.*, vol. 7, no. 3, pp. 537–568, 2009.
- [2] R. Evans *et al.*, "Patient experience and perceived acceptability of whole-body magnetic resonance imaging for staging colorectal and lung cancer compared with current staging scans: A qualitative study," *BMJ Open*, vol. 7, no. 9, 2017, Art. no. e016391.
- [3] D. Nicholls, J. Lee, H. Amari, A. J. Stevens, B. L. Mehdi, and N. D. Browning, "Minimising damage in high resolution scanning transmission electron microscope images of nanoscale structures and processes," *Nanoscale*, vol. 12, no. 41, pp. 21248–21254, 2020.
- [4] E. J. Candès *et al.*, "Compressive sampling," in *Proc. Int. Congr. Math.*, 2006, vol. 3, pp. 1433–1452.
- [5] M. Rani, S. Dhok, and R. Deshmukh, "A systematic review of compressive sensing: Concepts, implementations and applications," *IEEE Access*, vol. 6, pp. 4875–4894, 2018.
- [6] D. L. Donoho, "Compressed sensing," *IEEE Trans. Inf. Theory*, vol. 52, no. 4, pp. 1289–1306, Apr. 2006.
- [7] E. J. Candès, J. Romberg, and T. Tao, "Robust uncertainty principles: Exact signal reconstruction from highly incomplete frequency information," *IEEE Trans. Inf. Theory*, vol. 52, no. 2, pp. 489–509, Feb. 2006.
- [8] Y. Bao, Z. Tang, and H. Li, "Compressive-sensing data reconstruction for structural health monitoring: A machine-learning approach," *Struct. Health Monit.*, vol. 19, no. 1, pp. 293–304, 2020.
- [9] D. Zhao, F. Zhao, and Y. Gan, "Reference-driven compressed sensing MR image reconstruction using deep convolutional neural networks without pre-training," *Sensors*, vol. 20, no. 1, 2020, Art. no. 308.
- [10] M. J. Colbrook, V. Antun, and A. C. Hansen, "The difficulty of computing stable and accurate neural networks: On the barriers of deep learning and Smale's 18th problem," *Proc. Nat. Acad. Sci.*, vol. 119, no. 12, 2022, Art. no. e2107151119.
- [11] V. Antun, M. J. Colbrook, and A. C. Hansen, "Proving existence is not enough: Mathematical paradoxes unravel the limits of neural networks in artificial intelligence," *SIAM News*, vol. 55, no. 4, pp. 1–4, 2022. [Online]. Available: <https://sinews.siam.org/Details-Page/proving-existence-is-not-enough-mathematical-paradoxes-unravel-the-limits-of-neural-networks-in-artificial-intelligence>
- [12] C. Szegedy *et al.*, "Intriguing properties of neural networks," in *Proc. Int. Conf. Learn. Representations*, 2014.
- [13] S.-M. Moosavi-Dezfooli, A. Fawzi, and P. Frossard, "Deepfool: A simple and accurate method to fool deep neural networks," in *Proc. IEEE Conf. Comput. Vis. Pattern Recognit.*, 2016, pp. 2574–2582.
- [14] N. Akhtar and A. Mian, "Threat of adversarial attacks on deep learning in computer vision: A survey," *IEEE Access*, vol. 6, pp. 14410–14430, 2018.
- [15] N. Carlini and D. Wagner, "Audio adversarial examples: Targeted attacks on speech-to-text," in *Proc. IEEE Secur. Privacy Workshops*, 2018, pp. 1–7.
- [16] Y. Huang, T. Würfl, K. Breininger, L. Liu, G. Lauritsch, and A. Maier, "Some investigations on robustness of deep learning in limited angle tomography," in *Proc. Int. Conf. Med. Image Comput. Comput.- Assist. Interv.*, 2018, pp. 145–153.
- [17] V. Antun, F. Renna, C. Poon, B. Adcock, and A. C. Hansen, "On instabilities of deep learning in image reconstruction and the potential costs of AI," *Proc. Nat. Acad. Sci.*, vol. 117, no. 48, pp. 30088–30095, 2020.
- [18] S. G. Finlayson, J. D. Bowers, J. Ito, J. L. Zittrain, A. L. Beam, and I. S. Kohane, "Adversarial attacks on medical machine learning," *Science*, vol. 363, no. 6433, pp. 1287–1289, 2019.
- [19] A. Bastounis, A. C. Hansen, and V. Vlacic, "The mathematics of adversarial attacks in AI - Why deep learning is unstable despite the existence of stable neural networks," 2021, *arXiv:2109.06098*.
- [20] N. Gottschling, V. Antun, B. Adcock, and A. C. Hansen, "The troublesome kernel: Why deep learning for inverse problems is typically unstable," 2020, *arXiv:2001.01258*.
- [21] F. Knoll *et al.*, "Advancing machine learning for MR image reconstruction with an open competition: Overview of the 2019 fastMRI challenge," *Magn. Reson. Med.*, vol. 84, no. 6, pp. 3054–3070, 2020.
- [22] M. J. Muckley *et al.*, "State-of-the-art machine learning MRI reconstruction in 2020: Results of the second fastMRI challenge," 2020, *arXiv:2012.06318*.
- [23] B. Adcock, A. C. Hansen, C. Poon, and B. Roman, "Breaking the coherence barrier: A new theory for compressed sensing," in *Forum of Mathematics, Sigma*, vol. 5, Cambridge, U.K.: Cambridge Univ. Press, 2017.
- [24] C. Boyer, J. Bigot, and P. Weiss, "Compressed sensing with structured sparsity and structured acquisition," *Appl. Comput. Harmon. Anal.*, vol. 46, no. 2, pp. 312–350, 2019.
- [25] Y. Traonmilin and R. Gribonval, "Stable recovery of low-dimensional cones in Hilbert spaces: One RIP to rule them all," *Appl. Comput. Harmon. Anal.*, vol. 45, no. 1, pp. 170–205, 2018.
- [26] A. Bastounis and A. C. Hansen, "On the absence of uniform recovery in many real-world applications of compressed sensing and the restricted isometry property and nullspace property in levels," *SIAM J. Imag. Sci.*, vol. 10, no. 1, pp. 335–371, 2017. [Online]. Available: <https://doi.org/10.1137/15M1043972>

- [27] B. Adcock and A. C. Hansen, "Generalized sampling and infinite-dimensional compressed sensing," *Foundations Comput. Math.*, vol. 16, no. 5, pp. 1263–1323, 2016.
- [28] C. Li and B. Adcock, "Compressed sensing with local structure: Uniform recovery guarantees for the sparsity in levels class," *Appl. Comput. Harmon. Anal.*, vol. 46, no. 3, pp. 453–477, 2019.
- [29] Y. C. Eldar, P. Kuppinger, and H. Bolcskei, "Block-sparse signals: Uncertainty relations and efficient recovery," *IEEE Trans. Signal Process.*, vol. 58, no. 6, pp. 3042–3054, Jun. 2010.
- [30] B. Adcock, S. Brugiapaglia, and M. King-Roskamp, "Iterative and greedy algorithms for the sparsity in levels model in compressed sensing," in *Proc. SPIE Wavelets and Sparsity XVIII*, 2019, Art. no. 1113809.
- [31] L. Feng, T. Benkert, K. T. Block, D. K. Sodickson, R. Otazo, and H. Chandarana, "Compressed sensing for body MRI," *J. Magn. Reson. Imag.*, vol. 45, no. 4, pp. 966–987, 2017.
- [32] C. Boyer, P. Weiss, and J. Bigot, "An algorithm for variable density sampling with block-constrained acquisition," *SIAM J. Imag. Sci.*, vol. 7, no. 2, pp. 1080–1107, 2014.
- [33] F. Kraemer and R. Ward, "Stable and robust recovery from variable density frequency samples," *IEEE Trans. Image Process.*, vol. 23, no. 2, pp. 612–622, Feb. 2014.
- [34] B. Adcock and A. C. Hansen, *Compressive Imaging: Structure, Sampling, Learning*. Cambridge, U.K.: Cambridge Univ. Press, 2021. [Online]. Available: <https://books.google.co.uk/books?id=cAM0zgEACAAJ>
- [35] D. Nicholls *et al.*, "Compressive scanning transmission electron microscopy," in *Proc. IEEE Int. Conf. Acoust. Speech Signal Process.*, 2022, pp. 1586–1590.
- [36] A. Bastounis, A. C. Hansen, and V. Vlačić, "The extended Smale's 9th problem - On computational barriers and paradoxes in estimation, regularisation, computer-assisted proofs and learning," 2021, *arXiv:2110.15734*.
- [37] H. Nyquist, "Certain topics in telegraph transmission theory," *Trans. Amer. Inst. Elect. Eng.*, vol. 47, no. 2, pp. 617–644, 1928.
- [38] A. Koochakzadeh and P. Pal, "On the robustness of co-prime sampling," in *Proc. 23rd Eur. Signal Process. Conf.*, 2015, pp. 2825–2829.
- [39] P. Pal and P. P. Vaidyanathan, "Coprime sampling and the music algorithm," in *Proc. Digit. Signal Process. Signal Process. Educ. Meeting*, 2011, pp. 289–294.
- [40] T. Jia, H. Wang, X. Shen, and X. Liu, "Direction of arrival estimation with co-prime arrays via compressed sensing methods," in *Proc. OCEANS Shanghai*, 2016, pp. 1–5.
- [41] J. Fang, F. Wang, Y. Shen, H. Li, and R. S. Blum, "Super-resolution compressed sensing for line spectral estimation: An iterative reweighted approach," *IEEE Trans. Signal Process.*, vol. 64, no. 18, pp. 4649–4662, Sep. 2016.
- [42] L. Hu, Z. Shi, J. Zhou, and Q. Fu, "Compressed sensing of complex sinusoids: An approach based on dictionary refinement," *IEEE Trans. Signal Process.*, vol. 60, no. 7, pp. 3809–3822, Jul. 2012.
- [43] D. Mascareñas, A. Cattaneo, J. Theiler, and C. Farrar, "Compressed sensing techniques for detecting damage in structures," *Struct. Health Monit.*, vol. 12, no. 4, pp. 325–338, 2013.
- [44] Y. Yang and S. Nagarajah, "Output-only modal identification by compressed sensing: Non-uniform low-rate random sampling," *Mech. Syst. Signal Process.*, vol. 56, pp. 15–34, 2015.
- [45] Y. Bao, Z. Shi, X. Wang, and H. Li, "Compressive sensing of wireless sensors based on group sparse optimization for structural health monitoring," *Struct. Health Monit.*, vol. 17, no. 4, pp. 823–836, 2018.
- [46] D. Tcherniak and L. L. Mølgaard, "Active vibration-based structural health monitoring system for wind turbine blade: Demonstration on an operating vestas V27 wind turbine," *Struct. Health Monit.*, vol. 16, no. 5, pp. 536–550, 2017.
- [47] Y. Du, S. Zhou, X. Jing, Y. Peng, H. Wu, and N. Kwok, "Damage detection techniques for wind turbine blades: A review," *Mech. Syst. Signal Process.*, vol. 141, 2020, Art. no. 106445.
- [48] T. Loss, O. Gerler, and A. Bergmann, "Online calibration of accelerometers for monitoring of wind turbine blade movement," in *Proc. IEEE Int. Instrum. Meas. Technol. Conf.*, 2020, pp. 1–6.
- [49] L. Donati, M. Nilchian, S. Trépout, C. Messaoudi, S. Marco, and M. Unser, "Compressed sensing for STEM tomography," *Ultramicroscopy*, vol. 179, pp. 47–56, 2017.
- [50] H.-W. Kuo, A. E. Dorfi, D. V. Esposito, and J. N. Wright, "Compressed sensing microscopy with scanning line probes," 2019, *arXiv:1909.12342*.
- [51] V. Studer, J. Bobin, M. Chahid, H. S. Mousavi, E. Candes, and M. Dahan, "Compressive fluorescence microscopy for biological and hyperspectral imaging," *Proc. Nat. Acad. Sci.*, vol. 109, no. 26, pp. E1679–E1687, 2012.
- [52] C. S. Oxvig, T. Arildsen, and T. Larsen, "Structure assisted compressed sensing reconstruction of undersampled AFM images," *Ultramicroscopy*, vol. 172, pp. 1–9, 2017.
- [53] X. Liu, S. Zhang, A. Yurtsever, and J. Liang, "Single-shot real-time sub-nanosecond electron imaging aided by compressed sensing: Analytical modeling and simulation," *Micron*, vol. 117, pp. 47–54, 2019.
- [54] J. A. Don W. Fawcett, "Cil_36063, bombylius major, flight muscle cell," Accessed: Jan. 8, 2021. [Online]. Available: <http://www.cellimagelibrary.org/images/36063>
- [55] M. Guervos, "Cil_40405, convallaria majalis," Accessed: Jan. 8, 2021. [Online]. Available: <http://www.cellimagelibrary.org/images/40405>